Hindawi
Journal of Nanomaterials
Volume 2018, Article ID 9072325, 9 pages
https://doi.org/10.1155/2018/9072325

Research Article

Structural Characterization and Magnetic Properties of Undoped and Ti-Doped ZnO Nanoparticles Prepared by Modified Oxalate Route

Ekane Peter Etape,[1] **Josepha Foba-Tendo**,[1] **Lambi John Ngolui**,[2] **Beckley Victorine Namondo**,[1] **Fomogne Cyrille Yollande**,[1] **and Marius Borel Nguefack Nguimezong**[1]

[1]*Department of Chemistry, Faculty of Science, University of Buea, P.O. Box 63, Buea, Cameroon*
[2]*Department of Chemistry, ENS Yaoundé, BP 47, Yaoundé, Cameroon*

Correspondence should be addressed to Ekane Peter Etape; ekane20022001@yahoo.fr

Received 31 October 2017; Revised 14 January 2018; Accepted 6 February 2018; Published 22 March 2018

Academic Editor: Jean M. Greneche

Copyright © 2018 Ekane Peter Etape et al. This is an open access article distributed under the Creative Commons Attribution License, which permits unrestricted use, distribution, and reproduction in any medium, provided the original work is properly cited.

Ti-doped zinc oxide and pure zinc oxide nanoparticles were synthesized by a modified oxalate route using *Averrhoa carambola* fruit juice as a natural source of oxalate. The characteristics of the precursors have been investigated by FTIR, TGA, and XRD. The results from the investigation revealed that the precursors are zinc oxalate and Ti-doped zinc oxalate which readily decompose at 450°C. The as-prepared precursors were calcined at 450°C for 4 hours, and the decomposition products have been characterized by XRD, SEM, EDX, and VSM. XRD results revealed crystallinity with hexagonal wurtzite structure, while the average grain size was found to be 26 nm for Ti-doped ZnO and 29 nm for ZnO, using calculations based on Debye-Scherrer equation. Furthermore, the morphological studies by SEM showed particle agglomeration, while the presence of Ti^{3+} in the zinc oxide lattice is indicated by EDS analysis. Finally the hysteresis loop from VSM results shows that Ti-doped ZnO exhibits ferromagnetism.

1. Introduction

The magnetic properties of nanomaterials used in semiconductors seem to result from their ability to manipulate electron spins. These properties have been exploited in dilute magnetic semiconductor materials [1]. Zinc oxide is one of such materials that have received special interest because it has both charge and spin degrees of freedom in a single matrix, which lead to the interplay of functionalities (magnetic and electronic). Also the oxalates from the 3d metals such as zinc are isomorphous in nature, which enables the enhancement of physical properties of oxide semiconductors by doping the precursor in the course of synthesis [2–6]. Many research groups that have worked on doping with transition metals have used zinc oxide as a good host material for realizing wide band-gap dilute magnetic semiconductors. Furthermore, some special interest in titanium has been shown because neither titanium nor its oxides are ferromagnetic, but calculations of the electronic structure of Ti-doped ZnO have confirmed experimentally [7] and indicated the likelihood of titanium to order ferromagnetically in ZnO. However, to generate Ti-doped ZnO with good functional properties for industrial scale production, control of purity, morphology, size, and size distribution, and relatively simple and cost effective synthetic methods are required.

Several methods have been used for ZnO synthesis such as chemical precipitation in water solution [8], hydrothermal synthesis [9], sol-gel process [10], precipitation from microwave [11], and thermal evaporation [12] process. These methods have given products with particles differing in shape, size, and spatial structure. Metallurgical processes obtained zinc oxide from roasting of zinc ores as reported by the international organization for standardization (SIO). This method of synthesis is called the direct (American)

process or the indirect (French) process where zinc is melted in a furnace and vaporized at 910°C. This method was popularized by Le Claire in 1844, and the products consisted of agglomerations with average particle size ranging from 0.1 to a few microns [13]. The high temperatures involved make the process costly and this has encouraged the use of other methods operating at relatively lower temperatures. Also there is the mechanochemical process [14] which is cheap and simple, works at low temperature, and yields nanoparticles at an industrial scale, but uniform grinding of particles to the required size leads to longer processing time and greater quantity of impurities. The sol-gel methods reported have attracted a lot of interest in view of their simplicity, low cost, reliability, reproducibility, and relatively mild conditions of synthesis which make easy surface modification of zinc oxide with selected organic compounds. Benhebal et al., 2013, [15] produced zinc oxide powder by sol-gel method from zinc acetate dihydrate and oxalic acid, using ethanol as solvent. The zinc oxide obtained had a hexagonal wurtzite structure with the particles having a spherical shape, but the use of organic solvents makes the method relatively cost ineffective and environmentally questionable. Controlled precipitation is a widely used method for the generation of zinc and other metal oxide nanoparticles [16]. The method is fast and spontaneous, with the possibility of controlling particle size, but breaking down agglomerates remains a drawback [17]. Hong et al., 2006 [18], and Lanje et al. [19], 2013, reported on a cost effective and simple precipitation process for the synthesis of zinc oxide which could be used in the large scale production of pure zinc oxide particles. The microemulsion method [20] operates at low temperature 140°C and generates hexagonal (wurtzite) structure; particles morphology: needle (*L*: 150–200 nm, *D*: ~55 nm), nanocolumns (*L*: 80–100 nm, *D*: 50–80 nm), spherical shape (~45 nm). However, the conditions of the process (temperature, substrates, and ratio of two-phase components) affect the size of the particles and the location of their phases.

The modified solvothermal method using oxalate precursor has many advantages (it is cost effective and simple and produces pure and homogeneous nanoparticles [6]). However, a precipitation process which makes use of a natural source of precipitating agent could be more cost effective and environmentally appropriate. We have developed some special interest in the implementation of an environmentally friendly process which involves the use of renewable material sources such as fruit juices. Some of the fruit juices, like *Averrhoa carambola*, are very rich in organic acid (namely, oxalic acid), which can serve as ligand species for the precipitation of precursors for metal oxides. The concept is being developed and has proven to be an efficient one [21, 22]. In this paper, we follow the steps of our previous work [21, 22] and report for the first time the synthesis of doped metal oxide (Ti-doped ZnO) by a relatively low temperature method which involves the pyrolysis of a precursor by a coprecipitation route in aqueous solution using an oxalate ligand from a natural source (*A. carambola* fruit juice) as the precipitating agent. The nanoparticles have been characterized by powder X-ray diffraction, thermogravimetry, Fourier Transform Infrared (FTIR) spectroscopy, and scanning electron microscopy coupled to an EDAX, and magnetic properties have also been investigated.

Table 1: Quantitative and qualitative description of the various samples prepared.

Code	0.04 M $ZnCl_2$ (mL)	0.04 M $TiCl_3$ (mL)	*A. carambola* juice (mL)
ZZ	100	0	200
ZT	88	12	200

2. Experimental

2.1. Materials and Methods. Titanium trichloride (20% in 3% Hydrochloric acid) (Alfa Aesar, Germany) and zinc chloride (MERCK) were of analytical grade and were used without further purification. *Averrhoa carambola* juice (source of the precipitating agent) processed as described elsewhere [21] was also used.

2.1.1. Synthesis and Thermal Decomposition of Zinc and Titanium-Doped Zinc Oxalates. Zinc and titanium-doped zinc complexes (ZZ and ZT, where Z = Zn and T = Ti) were prepared from zinc chloride and titanium chloride using *Averrhoa carambola* juice as the source of the precipitating agent. 0.04 M solution of the various metal ions (Zn^{2+} and Ti^{3+}) was prepared by dissolving the appropriate amount of the metal chloride in 200 mL of distilled water. The metal ion solutions were then mixed in appropriate $Zn^{2+}:Ti^{3+}$ ratios (see Table 1) and stirred to homogenize. *Averrhoa carambola* fruit juice (see Table 1, for volumes) was poured into a 400 mL round bottom flask and maintained under magnetic stirring at ambient temperature. The metal ion solution was slowly added to the juice while stirring at room temperature and the mixture stirred for a further four hours. The solutions obtained (white for ZZ and greenish for ZT) were aged for eight (08) hours, filtered, washed successively with distilled water and ethanol, and then dried in an oven at 80°C for one hour. The decomposition products zinc oxide and titanium-doped zinc oxide (ZZd and ZTd, resp.) were obtained by calcination of the precursors zinc oxalate and titanium-doped zinc oxalate (ZZ and ZT resp.). ZZ and ZT were placed in ceramic combustion boat holders and maintained into a preheated muffle oven for four hours at 450°C under air. Table 1 gives a quantitative and qualitative description of the various samples prepared, and the flow chart of the synthesis is shown in Figure 1.

2.1.2. Characterization Techniques. Fourier Transform Infrared (FTIR) spectra were recorded from 4000 to 400 cm^{-1} on a PerkinElmer Spectrum Two Universal Attenuated Total Reflectance Fourier Transform Infrared (UATR-FTIR) spectrometer, while thermogravimetric analysis (TGA) was obtained using a Pyris 6 PerkinElmer TGA 4000 thermal analyzer. The TGA analysis was conducted between 30 and 900°C under nitrogen atmosphere at a flow rate of 20 mL/min and a temperature ramp of 10°C/min, while the XRD diffractogram of the precursors and the decomposition products

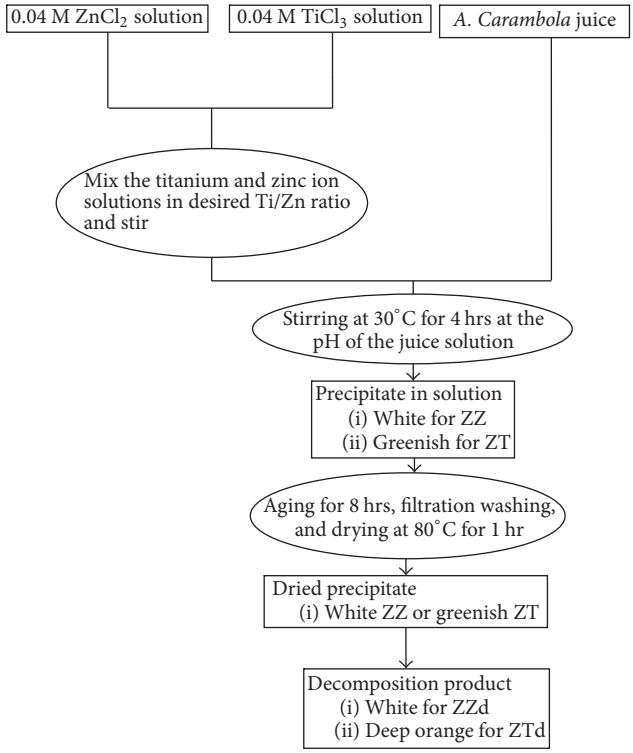


Figure 1: Flow diagram for the synthesis route of the materials.

were recorded on a Bruker D8 advance X-ray diffractometer using a Cu Kα radiation source (λ = 0.15406 nm, 40 kV, and 40 mA). Scans were taken over the 2θ range from 10°C to 100°C in steps of 0.01°C at room temperature in open quartz sample holders. The phases were identified with the help of a Bruker DIFFRAC plus evaluation software in combination with the ICDD (International Centre for Diffraction Data) powder diffraction database. The surface morphology of the samples was examined by a Scanning Electron Microscope (SEM) JEOL JSM-5600 while the elemental analysis was carried out using the same machine fitted with an EDAX DX-4 microanalysis system with an energy dispersive spectrometer (EDX). Prior to examination, samples were prepared by mounting about 0.5 mg of powder onto a 5 mm × 5 mm double sided carbon tape, on an aluminum stub. The powder was then sputter-coated for 40 seconds with gold. The magnetic measurement was performed on the commercial vibrating sample magnetometer (VSM) Lakeshore (model 73009). The magnetic hysteresis loops were measured at room temperature with maximal applied magnetic field up to 0.95 T. Magnetic field sweep rate was kept at 5 Oe/s so that the measurement of the hysteresis loop with maximum field of 0.989 t was taken from an interval of three hours. The saturation magnetization, coercivity, and remanent magnetization are obtained from hysteresis loop.

3. Results and Discursion

3.1. FTIR. Figure 2 Shows the FTIR spectra of oxalate precursors synthesized by coprecipitation using *A. Carambola*

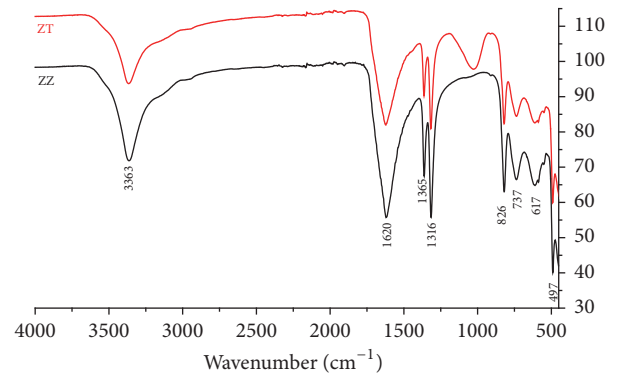
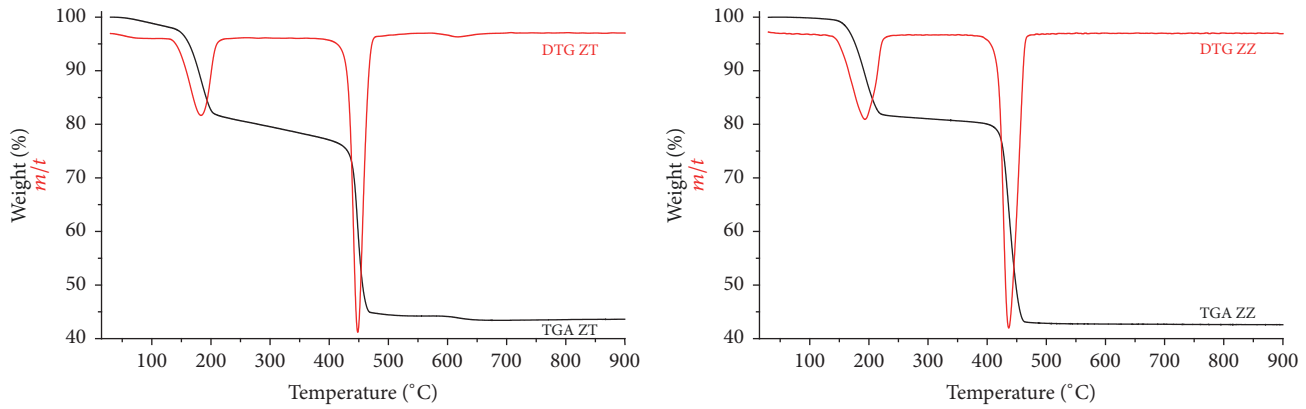


Figure 2: FTIR of the precursors: zinc complex (ZZ) and titanium-doped zinc complex (ZT).

fruit juice as precipitating agent. The spectra of the precursors (ZZ and ZT) are very similar with weak IR bands occurring around 3363 cm^{-1} corresponding to the stretching vibrations of the -OH group associated with the presence of water of crystallization. The presence of the water of crystallization is confirmed by the H-O-H bending vibration observed at 737 cm^{-1}. The Infrared bands observed below 1700 are assigned to the oxalate vibrational modes [21, 22] (the sharp intense peaks at 1620 cm^{-1} are attributed to the asymmetric stretching vibrations of the OCO group, while those around 1450–1300 cm^{-1} are attributed to the asymmetric (C=O) and symmetric (C-O) stretching vibrations in the OCO group). The sharp medium intense peaks at 826 cm^{-1} and 737 cm^{-1} confirm the bonding of metal oxygen (M-O) (indicating the presence of Zn^{2+} and Ti^{3+} bonded to the oxalate ion) and are assigned to ($V_{o\text{-}c=o}$ + $\delta_{Zn\text{-}O}$) and ($\delta_{Ti\text{-}O}$ + $V_{o\text{-}c=o}$). Moreover, the absence of the free IR $V_{C=O}$, vibration expected at 1735–1705 cm^{-1}, suggests that the entire carboxylate group of the oxalate is engaged in the formation of the coordination compound. On incorporating Ti^{+3} into the ZnO lattice sites, shifting of bands to lower wavenumbers is observed. This may be as a result of the bond weakening (increase in bond length) [23].

3.2. Thermal Analysis (TGA/DTG). The thermal decomposition of zinc oxalate (ZZ) and Ti-doped zinc oxalate (ZT) precursors was carried out within the same temperature range of 30–650°C (as shown in Figure 3). The decomposition of Ti_x-$Zn_{i-x}C_2O_4$ occurs in two steps (Figure 3(a)). The initial step is the dehydration process which takes place in two steps. The first step occurred in the temperature range 30–125°C (1) and the second step in the range 125–220°C (2). The dehydration steps for both the pure and the doped ZnC_2O_4 occurred within the same temperature range although the doped sample started dehydrating at a lower temperature, which revealed the relative instability of the doped crystal [23]. The measured weight loss for the first segment of the first step is about 4.5% of the total weight resulting in the elimination of half a molecule of water. The measured weight loss for the second segment of the first step is about 13.71%, which results in the elimination of one and a half molecules of water.



(a) Thermogram of Ti-doped zinc oxalate (ZT)

(b) Thermogram of zinc oxalate (ZZ)

Figure 3

The total weight of water of crystallization in the pure sample (19.02%) decreases (to 18.51%) following the incorporation of Ti^{+3} in the zinc oxalate crystal. This shows that on introducing titanium ion, water of crystallization decreases. The reduction in the water of crystallization could be attributed to H-bonding between the particles (on introducing Ti as dopant, the lattice contracts leading to a decrease in particle size and reduction in the H-bonding between the particles).

$$\mathrm{Ti}_x\text{-}\mathrm{Zn}_{1-x}\mathrm{C}_2\mathrm{O}_4 \cdot 2\mathrm{H}_2\mathrm{O} \longrightarrow \mathrm{Ti}_x\text{-}\mathrm{Zn}_{1-x}\mathrm{C}_2\mathrm{O}_4 \cdot \frac{3}{2}\mathrm{H}_2\mathrm{O} + \frac{1}{2}\mathrm{H}_2\mathrm{O} \quad (1)$$

$$\mathrm{Ti}_x\text{-}\mathrm{Zn}_{1-x}\mathrm{C}_2\mathrm{O}_4 \cdot \frac{3}{2}\mathrm{H}_2\mathrm{O} \longrightarrow \mathrm{Ti}_x\text{-}\mathrm{Zn}_{1-x}\mathrm{C}_2\mathrm{O}_4 + \frac{3}{2}\mathrm{H}_2\mathrm{O} \quad (2)$$

The second step, like the first, has also two segments. The first segment occurred in the temperature range 230–430°C and corresponds to the decomposition of the anhydrous doped oxalate, eliminating carbon monoxide (3). The last segment is the decarboxylation process, which occurred in the temperature range 430–650°C and constitutes the decomposition of the carbonate to the corresponding metal oxides (4).

$$\mathrm{Ti}_x\mathrm{Zn}_{1-x}\mathrm{C}_2\mathrm{O}_4 \longrightarrow \mathrm{Ti}_x\mathrm{Zn}_{1-x}\mathrm{CO}_3 + \mathrm{CO} \quad (3)$$

$$\mathrm{Ti}_x\mathrm{Zn}_{1-x}\mathrm{CO}_3 \longrightarrow \mathrm{Ti}_x\mathrm{Zn}_{1-x}\mathrm{O} + \mathrm{CO}_2 \quad (4)$$

Looking at the DTG, there is no apparent difference in the thermal decomposition patterns of the pure and the Ti added sample (ZT). Just like the Ti free sample (ZZ), the thermogram of ZT shows two well defined weight loss steps. Cong et al. [2] and Ahmad et al. [24] made similar observations for Mn-Zn oxalate. The first (19.29%) around 125–220°C is attributed to the loss of two molecules of water of crystallization (cf. 19.23%), while the second (36.80%) found between 400 and 480°C is attributed to the release of one molecule of each of CO_2 and CO (cf. 39.45%) giving a difference of 2.65%. The difference suggests that

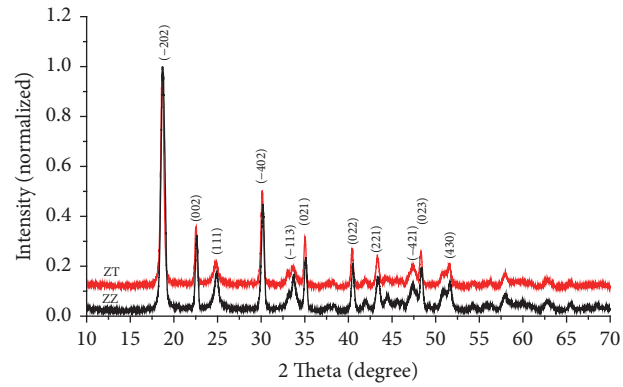


Figure 4: XRD of the precursors: zinc oxalate (ZZ) and Ti-doped zinc oxalate (ZT).

decomposition of ZT is not actually complete at 450°C. This observation could be attributed to the more stable $TiCO_3$ which holds back some proportion of CO_2. A closer view of the thermogram (TGA and DTG) for ZT reveals a little weight loss portion around 600°C which could accounts for the complete decomposition of ZT to ZTd. However calcinations of both ZZ and ZT at 450°C for 4 hours gives the final decomposition products (ZZd and ZTd).

3.3. XRD/EDS/SEM Characterization

3.3.1. X-Ray Diffraction. Figures 4 and 5 show, respectively, the room temperature powder X-ray diffraction spectra for the oxalate precursors (ZZ and ZT) and the decomposition products (ZZd and ZTd). All the reflections in the pattern could be indexed to the zinc oxalate (JCPDS card number 25-1029), Table 2, and monophasic zinc oxide hexagonal wurtzite structure (JCPDS card number 36-1451), Table 3, respectively. The diffraction patterns for sample ZZ and ZT are virtually indifferent and matched perfectly with JCPDS card number 25-1029 for zinc oxalate dehydrate. This is in conformity with FTIR results which indicated the presence

Table 2: PXRD data for the precursors (ZZ and ZT) indexed with JCPDS card number 25-1029 for zinc oxalate dehydrate.

JCPDS no. 25-1029		ZZ/ZT			
hkl	*d* (Å)	Intensity	2θ	*d* (Å)	Intensity
−202	4.77	100	18.27	4.85	100
002	3.6	35	22.83	3.89	31
−113	2.65	35	33.38	2.67	16
021	2.55	25	35.12	2.54	24
022	2.22	30	40.53	2.24	21
221	2.03	18	43.67	2.07	16
023	1.88	25	48.43	1.87	19

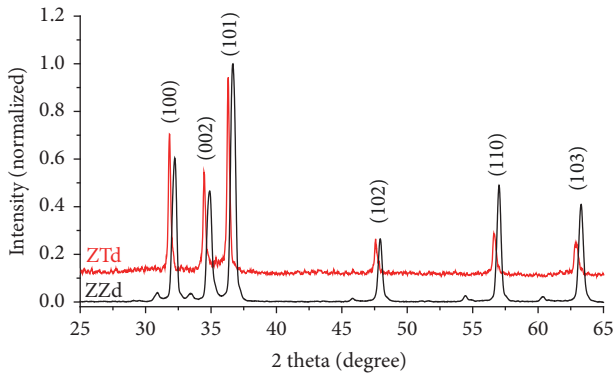


Figure 5: XRD of the decomposition products of the zinc complex (ZZd) and the titanium-doped zinc complex (ZTd).

of water of hydration. The peaks in the spectra of both ZZd and ZTd matched perfectly with JCPDS card number 36-1451 for hexagonal wurtzite ZnO structure, shown in Table 3. (No impurity peaks were observed as no peak from the patterns of the decomposed sample ZTd matched JCPDS card number 84-1286 for TiO_2 anatase phase and JCPDS card number 75-1753 rutile phase.) However, the diffraction peaks of Ti-doped ZnO are shifted to lower angles with respect to those of ZnO, which suggests some changes in the ZnO matrix resulting from the substitution of Ti for some Zn. The substitution is confirmed by the EDS spectrum shown in Figure 6, which shows that the composition of ZTd to be Ti, Zn, and O. Therefore, for the dopant proportion, Ti did not bring any change in the crystal structure of ZnO since there was complete incorporation of Ti into the ZnO structure by substituting for some of the Zn. This phenomenon was earlier observed by other groups for Ti-doped ZnO nanoparticle [25] and films [2], and they attributed the shift in 2θ values to a distortion of the ZnO crystallite when Ti substitutes for Zn since Ti^{4+} radius is lower than that of Zn^{2+}. Therefore, the formula of ZTd and ZZd could be written as $Zn_{0.958}Ti_{0.042}O$ and ZnO, respectively. The crystallite size was estimated from X-ray line broadening studies using (101) reflections with the help of the Debye-Scherer's equation (5) and was found to be 29 nm and 26 nm for pure and doped ZnO, respectively.

$$D = \frac{k\lambda}{\beta \cos\theta}, \tag{5}$$

where D is the crystallite size, k is the correction factor that accounts for the shape of the particles, λ is the wavelength of the XRD beam (here $\lambda = 0.15406$ nm), β is the full width at half maximum (FWHM) of the peak, and θ is the Bragg's diffraction angle

The SEM images of ZZd (ZnO) and ZTd (Ti-doped ZnO) are shown in Figures 7(a) and 7(b). A high degree of particle agglomeration is observed, which is in agreement with literature [2]. The SEM images for the calcined products at 450°C for 4 hours are shown in Figures 7(c) and 7(d). On the one hand, ZZd (ZnO) is present as regular polyhedral particles with the hexagonal shape of the wurtzite structure observed in PXRD, while, on the other hand, ZTd (Ti-doped ZnO) shows spherical particulates with some level of agglomeration and an average agglomerate size of about 2 μm in width and 4 μm in length. The fact that agglomerates showed sizes in the range of 2 μm indicates that the particulates are in the nanometer range which conforms to the XRD results.

3.4. Vibrating Sample Magnetometry (VSM). The magnetic behavior of the nanoparticles was investigated by plotting the magnetic moment as a function of the applied magnetic field measured at a temperature of 5 k while the magnitudes of the magnetic properties obtained from the hysteresis loop are shown in Table 4. The observed curve shows a hysteresis (Figure 8), which indicates the existence of ferromagnetic ordering in the sample. The solid solution shows saturated magnetization (M_s) of 6.89 emu/g, remnant magnetization (M_r) of 7.93 emu/g at room temperature, and a coercive force (H_c) of ZTd of 1.500 (Oe) which could be attributed to the tiny nature of the as-prepared ZTd particles [26, 27]. The squareness (remanence ratio) M_r/M_s for the sample was determined and the value obtained was 0.012.

The experimental magnetic moment was calculated using the equation

$$\eta = M_w \times \frac{M_s}{5585}. \tag{6}$$

M_w is the molecular weight of the sample while M_s is the saturation magnetization (emu/g) [28]. The value of the magnetic moment obtained was 0.1004 emu for 4.2% Ti-doped ZnO compared with saturation magnetic moment of about 0.15 $\mu\beta$/Ti atom at room temperature for 5% Ti-doped ZnO [4]. Similar existence of ferromagnetism has been observed earlier in Fe-doped ZnO [29] and Mn-doped ZnO [30].

The particle size of 26 nm obtained was less than the critical nanoparticle size (100 nm); consequently the nanoparticles form single domains with all the spins aligned in the same direction and uniformly magnetized. Furthermore, because there are no domain walls to move, the magnetization will be reversed through spin rotation rather than through the motion of domain walls which results in large coercivity of

Table 3: PXRD data for the decomposition products (ZZd and ZTd) indexed with JCPDS card number 36-1451 for wurtzite ZnO.

JCPDS no. 36-1451 ZnO wurtzite structure		ZZd		ZTd	
2θ	hkl	2θ	Relative intensity	2θ	Relative intensity
31.749	100	31.8	71.7	32.307	58.85
34.228	002	34.46	50.94	34.82	48.83
36.257	101	36.3	100	36.6	100
47.257	102	47.62	19.81	48.02	26.68
	110	56.66	19.81	57.15	46.72
	103	62.94	18.87	63.25	38.71

Table 4: The magnitudes of the magnetic properties obtained from the hysteresis loop.

Hysteresis loop	Upward part	Downward part	Average	Parameter "definition"
H_c Oe	−9999.000	−9996.000	−1.500	Coercive field, field at which $M//H$ change sign
M_r emu	$-11.181E-6$	$4.673E-6$	$7.927E-6$	Remanent magnetization: M at $H = 0$
S	0.016	0.008	0.012	Squareness: M_r/M_s
S^*	1.005	1.013	1.009	$1 - (M_r/H_c)$ (1 slope at H_c)
M_s emu	$689.246E-6$	$-615.022E-6$	$652.134E-6$	Saturation magnetization: maximum M measured
M at H_{max} emu	$-615.022E-6$	$6899.246E-6$	$652.134E-6$	M at the maximum field
Permeability, CGS-slope [ur]	$984.957E-3$	$985.307E-3$	$985.132E-3$	Permeability calculated from slope in CGS (unit less) requires correct volume in sample dimensions
H_s Oe	−9999.00	−9996.00	9997.50	Saturation field, field at which M reaches $0.95M_s$
H_{max} Oe	10002.000	−9999.000	10000.500	Maximum H measured

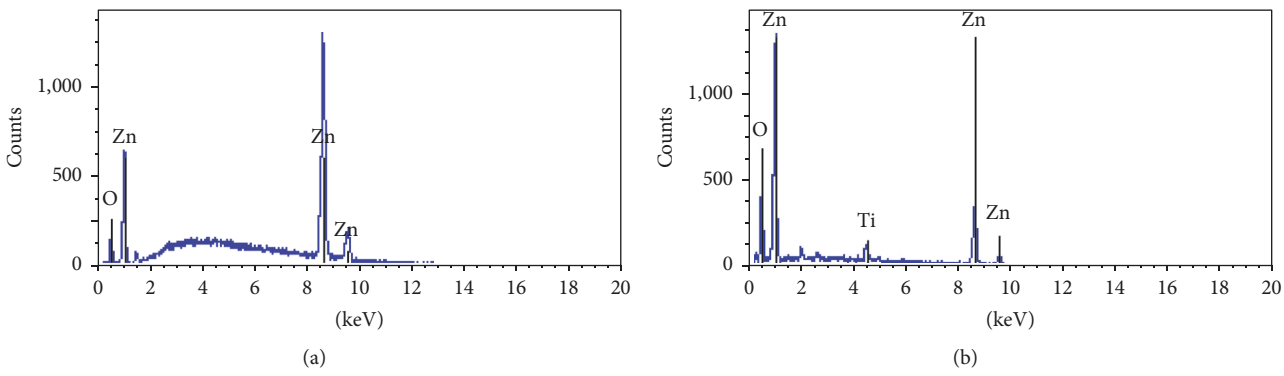
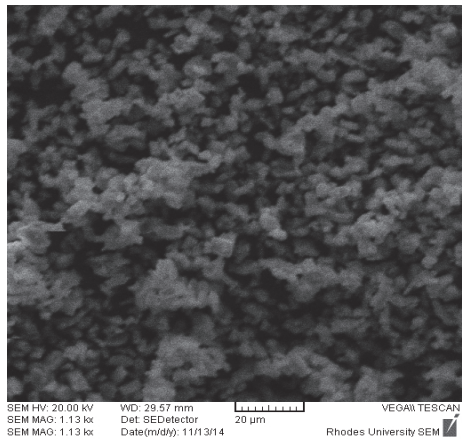


Figure 6: The EDS of the decomposition products, zinc oxide (ZZd), and the titanium-doped zinc oxide (ZTd).

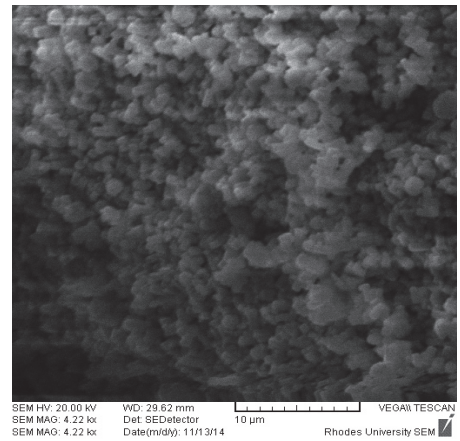
the nanoparticles. However observed coercivity (magnetic field required to bring the magnetization back to zero) of 1.500 (Oe) is relatively small suggesting that the nanoparticles are spherical. This observation is in conformity with the SEM results which suggested that the Ti-doped ZnO nanoparticles were spherical. At such low coercivity, the ferromagnetic nanoparticles with possible coexistence of paramagnetism behave like paramagnetic atoms with giant spins, and as the coercivity turns to zero, the nanoparticles become super magnetic [20, 31].

4. Conclusion

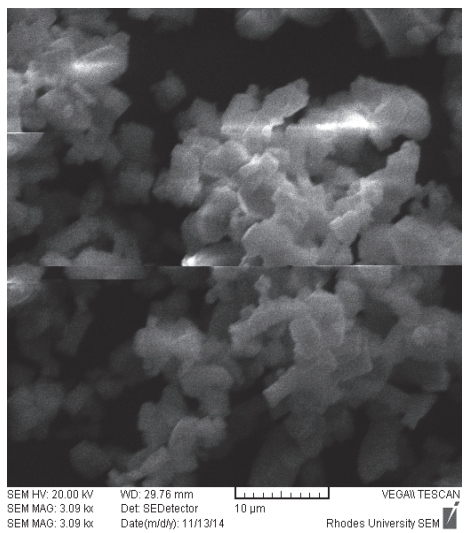
Pure nanocrystalline ZnO (29 nm) and Ti-doped ZnO (26 nm) dilute magnetic semiconductors have been successfully synthesized by a modified oxalate process for the first



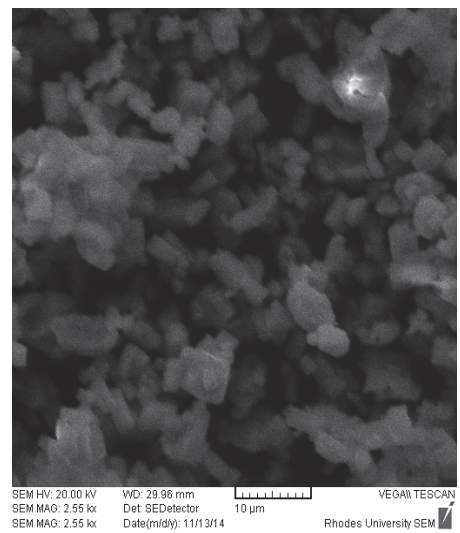
(a) SEM image of ZZd (ZnO)



(b) SEM image of ZTd (Ti-doped ZnO)

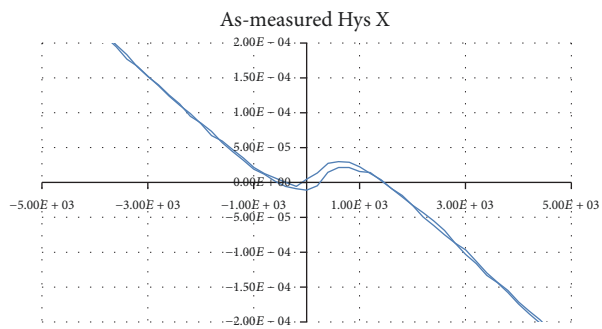


(c) SEM image of calcined, ZZd (ZnO)

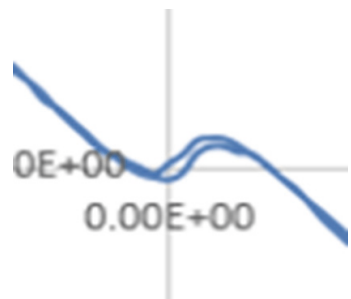


(d) SEM image of calcined, ZTd (Ti-doped ZnO)

Figure 7



(a) Magnetization versus the applied field plot at room temperature for the obtained power Ti-doped ZnO (ZTd)



(b) Zoomed-in image of Figure 8(a)

Figure 8

time, using *Averrhoa carambola* fruit juice as the source of the precipitating agent. The precursors were identified as the expected metal oxalates, and the decomposition products were found to be pure ferromagnetic nanoparticles.

Our results demonstrate that not only the proposed modified coprecipitation technique, by using a precipitating agent extract from *A. Carambola* juice, is simple, environmentally friendly, low-cost, controllable, but it can also be applied to

prepare spherical Ti-doped ZnO magnetic nanoparticles and possibly a wide variety of mixed metal oxides useful in many applications.

Conflicts of Interest

The authors declare that there are no conflicts of interest regarding the publication of this article.

References

[1] X. Ma and C. Lou, "The dilute magnetic and optical properties of Mn-doped ZnO nanowires," *Journal of Nanomaterials*, vol. 2011, Article ID 464538, 5 pages, 2011.

[2] C. J. Cong, L. Liao, J. C. Li, L. X. Fan, and K. L. Zhang, "Synthesis, structure and ferromagnetic properties of Mn-doped ZnO nanoparticles," *Nanotechnology*, vol. 16, no. 6, pp. 981–984, 2005.

[3] C. J. Cong, L. Liao, Q. Y. Liu, J. C. Li, and K. L. Zhang, "Effects of temperature on the ferromagnetism of Mn-doped ZnO nanoparticles and Mn-related Raman vibration," *Nanotechnology*, vol. 17, no. 5, pp. 1520–1526, 2006.

[4] S. Thota, T. Dutta, and J. Kumar, "On the sol-gel synthesis and thermal, structural, and magnetic studies of transition metal (Ni, Co, Mn) containing ZnO powders," *Journal of Physics: Condensed Matter*, vol. 18, no. 8, pp. 2473–2486, 2006.

[5] B. V. Donkova, K. I. Milenova, and D. R. Mehandjiev, "Investigation on the catalytic activity of doped low-percentage oxide catalysts Mn/ZnO obtained from oxalate precursor," *Central European Journal of Chemistry*, vol. 6, no. 1, pp. 115–124, 2008.

[6] T. Ahmad, S. Khatoon, and K. Coolahan, "Optical, magnetic and structural characterization of Zn 1-xCoxO nanoparticles synthesized by solvothermal method," *Bulletin of Materials Science*, vol. 36, no. 6, pp. 997–1004, 2013.

[7] K. Osuch, E. B. Lombardi, and W. Gebicki, "First principles study of ferromagnetism in Ti0.0625 Zn0.9375 O," *Physical Review B: Condensed Matter and Materials Physics*, vol. 73, no. 7, Article ID 075202, 2006.

[8] M. G. Nair, M. Nirmala, K. Rekha, and A. Anukaliani, "Structural, optical, photo catalytic and antibacterial activity of ZnO and Co doped ZnO nanoparticles," *Materials Letters*, vol. 65, no. 12, pp. 1797–1800, 2011.

[9] D.-T. Phan and G.-S. Chung, "Effects of defects in Ga-doped ZnO nanorods formed by a hydrothermal method on CO sensing properties," *Sensors and Actuators B: Chemical*, vol. 187, pp. 191–197, 2013.

[10] N. Talebian, M. R. Nilforoushan, and E. B. Zargar, "Enhanced antibacterial performance of hybrid semiconductor nanomaterials: ZnO/SnO2 nanocomposite thin films," *Applied Surface Science*, vol. 258, no. 1, pp. 547–555, 2011.

[11] R. Jalal, E. K. Goharshadi, M. Abareshi, M. Moosavi, A. Yousefi, and P. Nancarrow, "ZnO nanofluids: green synthesis, characterization, and antibacterial activity," *Materials Chemistry and Physics*, vol. 121, no. 1-2, pp. 198–201, 2010.

[12] Q. Li, Y. Chen, L. Luo, L. Wang, Y. Yu, and L. Zhai, "Photoluminescence and wetting behavior of ZnO nanoparticles/nanorods array synthesized by thermal evaporation," *Journal of Alloys and Compounds*, vol. 560, pp. 156–160, 2013.

[13] S. Mahmud, M. J. Abdullah, G. A. Putrus, J. Chong, and A. K. Mohamad, "Nanostructure of ZnO fabricated via French process and its correlation to electrical properties of semiconducting varistors," *Synthesis and Reactivity in Inorganic, Metal-Organic, and Nano-Metal Chemistry*, vol. 36, no. 2, pp. 155–159, 2006.

[14] W. Ao, J. Li, H. Yang, X. Zeng, and X. Ma, "Mechanochemical synthesis of zinc oxide nanocrystalline," *Powder Technology*, vol. 168, no. 3, pp. 148–151, 2006.

[15] H. Benhebal, M. Chaib, T. Salmon et al., "Photocatalytic degradation of phenol and benzoic acid using zinc oxide powders prepared by the sol-gel process," *Alexandria Engineering Journal*, vol. 52, no. 3, pp. 517–523, 2013.

[16] R. L. Fomekong, P. K. Tsobnang, D. Magnin, S. Hermans, A. Delcorte, and J. L. Ngolui, "Coprecipitation of nickel zinc malonate: A facile and reproducible synthesis route for Ni1xZnxO nanoparticles and Ni1xZnxO/ZnO nanocomposites via pyrolysis," *Journal of Solid State Chemistry*, vol. 230, Article ID 19013, pp. 381–389, 2015.

[17] R. Lontio Fomekong, J. Ngolui Lambi, G. R. Ebede et al., "Effective reduction in the nanoparticle sizes of NiO obtained via the pyrolysis of nickel malonate precursor modified using oleylamine surfactant," *Journal of Solid State Chemistry*, vol. 241, pp. 137–142, 2016.

[18] R. Hong, T. Pan, J. Qian, and H. Li, "Synthesis and surface modification of ZnO nanoparticles," *Chemical Engineering Journal*, vol. 119, no. 2-3, pp. 71–81, 2006.

[19] A. S. Lanje, S. J. Sharma, R. S. Ningthoujam, J.-S. Ahn, and R. B. Pode, "Low temperature dielectric studies of zinc oxide (ZnO) nanoparticles prepared by precipitation method," *Advanced Powder Technology*, vol. 24, no. 1, pp. 331–335, 2013.

[20] X. Li, G. He, G. Xiao, H. Liu, and M. Wang, "Synthesis and morphology control of ZnO nanostructures in microemulsions," *Journal of Colloid and Interface Science*, vol. 333, no. 2, pp. 465–473, 2009.

[21] N. N. M. Borel, J. Foba-Tendo, D. M. Yufanyi, E. P. Etape, J. N. Eko, and L. J. Ngolui, "*Averrhoa carambola*: a renewable source of oxalic acid for the facile and green synthesis of divalent metal (Fe, Co, Ni, Zn, and Cu) oxalates and oxide nanoparticles," *Journal of Applied Chemistry*, vol. 2014, Article ID 767695, 9 pages, 2014.

[22] E. P. Etape, L. J. Ngolui, J. Foba-Tendo, D. M. Yufanyi, and B. V. Namondo, "Synthesis and characterization of CuO, TiO_2, and CuO-TiO_2 mixed oxide by a modified oxalate route," *Journal of Applied Chemistry*, vol. 2017, Article ID 4518654, 10 pages, 2017.

[23] T. Ahmad, S. Khatoon, K. Coolahan, and S. E. Lofland, "Structural characterization, optical and magnetic properties of Ni-doped CdO dilute magnetic semiconductor nanoparticles," *Journal of Materials Research*, vol. 28, no. 9, pp. 1245–1253, 2013.

[24] T. Ahmad, S. Khatoon, and O. A. Al-Hartomy, "Solvothermal synthesis of Zn1−xMnxO nanoparticles using oxalate precursor route: Optical and magnetic properties," *Arabian Journal of Chemistry*, vol. 10, pp. S2138–S2144, 2017.

[25] Y.-C. Tseng, Y.-J. Lin, H.-C. Chang, Y.-H. Chen, C.-J. Liu, and Y.-Y. Zou, "Effects of Ti content on the optical and structural properties of the Ti-doped ZnO nanoparticles," *Journal of Luminescence*, vol. 132, no. 2, pp. 491–494, 2012.

[26] Z.-Y. Ye, H.-L. Lu, Y. Geng et al., "Structural, electrical, and optical properties of Ti-doped ZnO films fabricated by atomic layer deposition," *Nanoscale Research Letters*, vol. 8, no. 108, 6 pages, 2013.

[27] E. C. Stoner and E. P. Wohlfarth, "A mechanism of magnetic hysteresis in heterogeneous alloys," *Philosophical Transactions*

of the Royal Society A: Mathematical, Physical & Engineering Sciences, vol. 240, no. 826, pp. 599–642, 1948.

[28] M. M. El-Okr, M. A. Salem, M. S. Salim, R. M. El-Okr, M. Ashoush, and H. M. Talaat, "Synthesis of cobalt ferrite nanoparticles and their magnetic characterization," *Journal of Magnetism and Magnetic Materials*, vol. 323, no. 7, pp. 920–926, 2011.

[29] G. Y. Ahn, S.-I. Park, I.-B. Shim, and C. S. Kim, "Mössbauer studies of ferromagnetism in Fe-doped ZnO magnetic semiconductor," *Journal of Magnetism and Magnetic Materials*, vol. 282, no. 1-3, pp. 166–169, 2004.

[30] O. D. Jayakumar, I. K. Gopalakrishnan, R. M. Kadam, A. Vinu, A. Asthana, and A. K. Tyagi, "Magnetization and structural studies of Mn doped ZnO nanoparticles: Prepared by reverse micelle method," *Journal of Crystal Growth*, vol. 300, no. 2, pp. 358–363, 2007.

[31] S. Bedanta and W. Kleemann, "Supermagnetism," *Journal of Physics D: Applied Physics*, vol. 42, no. 1, Article ID 013001, 2009.